Motion response induced by air cushioning effect during the water impact of a plate at small deadrise angles

Xiaohang Shi, Qiulin Qu,[*] Peiqing Liu, Yunlong Zheng, and Hao Guo
Institute of Fluid Mechanics, Beihang University, Beijing 100191, China

When a flat plate impacts water at small deadrise angles, the air cushion underneath plate bottom is asymmetrical about plate center and produces great asymmetrical impact pressure. In such an occasion, the motion response of plate should be very complicated and is highly coupled with air cushioning effect, particularly, the pitching motion which will alter the transient deadrise angle. However, the existing studies only considered the vertical translational motion, both the horizontal translational motion and pitching motion are restricted. In this paper, the complete motion behavior of plate induced by air cushioning effect during the water impact at small deadrise angles is numerically studied. In the regime of impact velocity and deadrise angle, four typical plate motion patterns have been discovered based on the variation characteristics of pitch angle: pitching-down, fluctuating-pitching-down, pitching-up-down, and pitching-up. To elucidate the underlying mechanism, the water impact process of plate at small deadrise angles is investigated, which contains four distinct stages: keel compression, edge compression, fluid expansion, and reloading. The pitching motion patterns are mainly determined by the keel compression and edge compression stages. In the keel compression stage, the air underneath plate keel is compressed and produces a pitching-down moment; in the following edge compression stage, the air underneath plate edge is heavily compressed and produces a strong pitching-up moment. Further, the influence of impact velocity and deadrise angle on the pitching motion has been investigated.

I. INTRODUCTION

Water impact phenomenon is widely seen in many industrial processes, such as ship hull or bottom slamming, the cross member or wet-deck slamming in offshore platforms, emergency ditching of aircraft, spacecraft falling into water upon return, underwater weapons, and underwater vehicles upon launch [1–5]. These complicated processes are generally studied by the water impact of simple objects with typical cross-section shapes such as a wedge [6,7], cylinder [8], or flat plate [9–12] to focus on their typical flow features. This paper will focus on the flat-plate impact problems characterized by air cushioning phenomenon.

Early research on the subject was initiated by von Kármán [13], who applied momentum theory to estimate water impact forces on a 2D wedge; then, the work was complemented by Wagner [14] by considering water pile-up effects. Years of research found that Wagner's theory cannot be applied to small deadrise angles due to the air cushioning phenomenon [15–17]. For water impact of shallow wedges and flat-bottom structures, an air layer is often entrapped beneath their lower surface. The trapped air not only cushions the transient impact load and prolongs impact time, but also alters load

---
[*]Corresponding author: qql@buaa.edu.cn

distributions greatly. There is a general agreement that the air cushioning effect occurs at zero and small deadrise angles (usually no more than 3° [15,16,18]).

To gain an insight into the general physics of air cushioning phenomenon, previous studies have focused mainly on the water impact of a flat plate at zero-deadrise angle, and some common understandings have been reached [10,11,19–21]. Based on the time-history characteristics of impact load on plate, the impact process can be divided into three distinctive stages: shock load stage with a high-pressure peak, fluid expansion stage with very low subatmospheric pressure, and less severe reloading stage [19,22,23]. The variation of impact load is correlated with the compression-expansion behavior of the trapped air. Specifically, at shock load stage, the trapped air is extensively compressed and the pressure increases; at fluid expansion stage, the compressed air expands, thus the pressure drops; and at reloading stage, the air repeats the compression-expansion processes periodically, exerting pulsating loads on the plate. Spatially, both the trapped air bubbles underneath plate bottom [20,24–27] and the flow behavior [11,19] are almost symmetric about plate center. As a consequence, the impact pressure distribution on the plate bottom is nearly symmetric [15,19] and the plate basically only performs translational motion in the vertical direction [28].

Research on the small deadrise angles condition is relatively limited. This scenario is of practical interest as there are inevitably some disturbances in either the attitude of impact model or water surface environment. Under this circumstance, the air cushioning effect differs significantly from that of zero-deadrise angle condition. Bagg *et al.* [16] studied the spatial distribution of trapped air bubbles under wedges of small deadrise angles. They identified that the air bubbles are mainly localized under the edge area of wedge, while the keel area basically traps no air. It was also claimed that the air cushioning effect is very sensitive to deadrise angle, i.e., a slight increase in the deadrise angle causes a significant reduction in the amount of trapped air. Chuang [18] reported that for the deadrise angles over 3°, most of the trapped air is pushed aside before the wedge keel approaching water surface, and hence the air cushioning effect is only non-negligible when the deadrise angle is very small. The same phenomenon was reported by Abrahamsen *et al.* [24] for the water impact experiment of flat plate. Okada and Sumi [15] measured the pressure distribution on a flat plate impacting water at small deadrise angles, showing highly spatial asymmetries about plate center. Under this circumstance, except for the vertical impact force component, both the horizontal impact force component and pitching moment can be huge. As a response, the plate is expected to perform horizontal translational motion and pitching motion during the descending process. Particularly, the pitching motion will change the instantaneous deadrise angle and affect the air cushioning effect in turn. Hence, the dynamic coupling process between air cushioning effect and plate-pitching motion should be considered.

While about the motion response of the plate impacting water at small deadrise angles, the existing studies [15–18,24] only considered the vertical translational motion. Figure 1 shows the typical experimental setup on water impact experiments [15]. The plate is first adjusted to a certain angle and then slides along the rail to impact water surface. During the whole water entry process, the plate only can perform vertical translational motion due to the rail restriction. Thus, the dynamic coupling process between air cushioning effect and plate-pitching motion cannot be reproduced.

For the water impact of plate at small deadrise angles, what motion behavior of plate will occur, how does it vary with impact conditions, e.g., the impact velocity and deadrise angle, and the responsible physical mechanism are all unknown. This paper will use numerical techniques to systematically investigate these problems, which might provide an insight into the motion response induced by air cushioning effect.

II. NUMERICAL METHOD AND VALIDATION

A. Numerical method

In this section, the numerical method, including the capture of free surface, the coupling of fluid dynamics and plate rigid-body kinematics, and the dynamic mesh technique for relative motion between plate and free surface is briefly described.
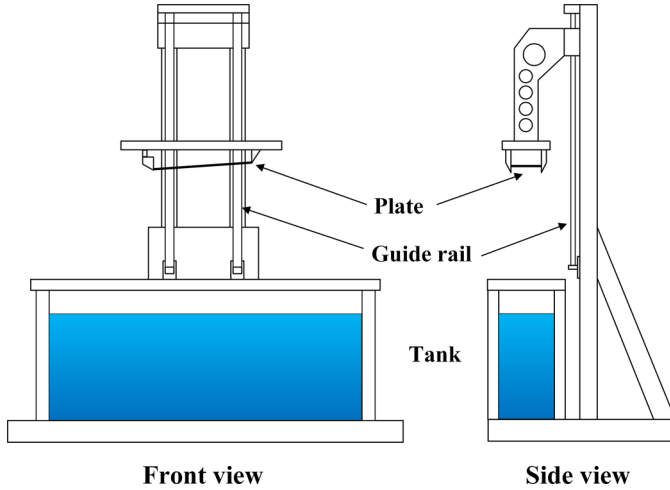
FIG. 1. Schematic of typical experimental setup on water impact of flat plate at small deadrise angles (adapted from Ref. [15]; it is redrawn here for clarity).

1. Flow solver

The simulation is performed on the open-source numerical coding platform OPENFOAM, by solving the unsteady compressible Reynolds-averaged Navier-Stokes equations with the shear-stress transport k-ω turbulence model. For the air cushioning study, the fluid compressibility has to be considered based on twofold reasons. First, the water impact of flat plate is characterized by the strong compression-expansion behavior of trapped air. Second, the speed of escaping air near plate edge is pretty high and far beyond the incompressible velocity range. As such, the existing two-phase flow solver COMPRESSIBLEINTERFOAM is adopted, which is developed for two compressible immiscible fluids using the volume-of-fluid (VOF) method for interface capturing.

The PIMPLE algorithm, i.e., a combination of the PISO (pressure-implicit split-operator) algorithm and SIMPLE (semi-implicit method for pressure-linked equations) algorithm, is selected to deal with the pressure-velocity coupling. The unsteady terms are discretized by the Euler scheme, a first-order implicit scheme. The gradient terms are discretized by the Gauss linear scheme, a second-order central difference scheme. The convection terms in momentum equation and turbulence equation are discretized by the Gauss vanLeerV and limitedLinear schemes of second-order accuracy, respectively. For the diffusion term, Gauss linear orthogonal scheme is used with second-order accuracy.

2. Volume of fluid method

The VOF method was proposed by Hirt and Nichols [29] and can capture the free interfaces between two or more immiscible fluids by introducing a variable, called volume fraction, for each phase. If the volume fraction of the qth fluid in a certain cell is denoted as α_q: $\alpha_q = 0$ indicates that the cell is empty of the qth fluid; $\alpha_q = 1$ indicates that the cell is full of the qth fluid; and $0 < \alpha_q < 1$ means that the cell contains the interface between the qth fluid and other fluids. The sum of the volume fractions of all phases must be 1 in each cell. The volume-fraction equation (the continuity equation) of the qth fluid is written as follows:

$$\frac{\partial}{\partial t}(\alpha_q \rho_q) + \nabla(\alpha_q \rho_q \boldsymbol{v}_q) = 0. \tag{1}$$
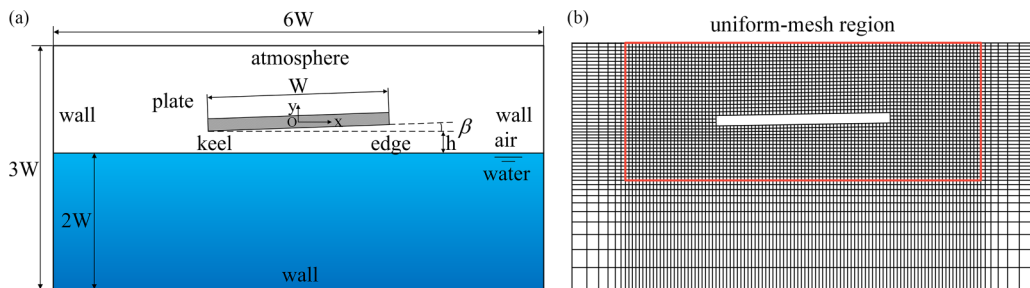
FIG. 2. Schematic of (a) computational domain and global coordinate system and (b) the whole mesh layout with every 20 grid points shown for clarity.

3. Six degree of freedom model

The sixDoFRigidBodyMotion solver is adopted to deal with the coupling of fluid dynamics and plate rigid-body kinematics. The translational motion equation is solved in the global coordinate system to obtain the motions of center of gravity (CG). The rotational motion equation is solved in the body-fixed coordinate system to obtain the attitude of plate.

$$\dot{\boldsymbol{v}}_g = \frac{1}{m} \sum \boldsymbol{f}_g, \tag{2}$$

$$\dot{\boldsymbol{\omega}} = K^{-1} \left(\sum \boldsymbol{M} - \boldsymbol{\omega} \times K\boldsymbol{\omega} \right), \tag{3}$$

where $\boldsymbol{v}_g$ and $\boldsymbol{\omega}$ are the translational and rotational angular velocity, m and K are the mass and moment of inertia, and $\boldsymbol{f}_g$ and $\boldsymbol{M}$ are the resultant force and moment, respectively. In this paper, a two-dimensional (2D) flat plate is adopted; thus, the plate has three degree of freedom motion, i.e., horizontal and vertical translations, and rotation about CG.

4. Global moving-mesh method

The global moving-mesh (GMM) method [30] is used to deal with the relative motion between plate and free water surface. The GMM method allows the whole computational domain (including the cells and boundaries) to move together with plate. It moves the entire mesh rigidly along with the plate at each time step according to the solution of sixDoFRigidBodyMotion solver. The volume-fraction boundary condition can ensure the free water surface maintains a given level when the computational domain moves. This condition is set using the *setFieldsDict* tool, which creates a bounding box to define the cells of water region according to the cell coordinates in the global coordinate system, and the phase fraction α_{water} is defined as 1 in this region. By using the GMM method, there is no need to adopt any remeshing or deformation techniques, thereby improving the accuracy of free water-surface capture.

B. Physical model and mesh

In this paper, a 2D flat plate is adopted. The plate width is set as $W = 0.5$ m and height is set as 0.03 m, referring to the cross section of flat-bottom structure in Ref. [31]. The plate has the same material property of steel with density of 7850 kg/m^3, and the pitching moment of inertia about CG per unit length is 2.462 kgm^2 (the length orientation is perpendicular to the page). The densities of air and water are 1.225 and 998.2 kg/m^3, respectively, and the dynamic viscosities are 1.813×10^{-5} and 9.982×10^{-4}Pas. The surface tension between air and water is set as $\sigma = 7.07 \times 10^{-2}$N/m.

Figure 2(a) depicts the global coordinate system and computational domain. The origin O is located at the initial CG position of plate, where the positive direction of the x axis is horizontally to right, and the positive direction of the y axis is vertically upwards. The deadrise angle β is defined

TABLE I. Parameters used in the simulation.

Parameters	Values
Initial deadrise angle β_0 (°)	0, 1, 2, 3, 4
Impact velocity V_0 (m/s)	1, 1.5, 2, 3, 4, 5, 6, 7
Froude number Fr	0.45, 0.68, 0.90, 1.35, 1.81, 2.26, 2.71, 3.16
Reynolds number Re ($\times 10^6$)	0.5, 0.75, 1.0, 1.5, 2.0, 2.5, 3.0, 3.5
Weber number We ($\times 10^4$)	0.71, 1.59, 2.82, 6.35, 11.3, 17.6, 25.4, 34.6

as angle between lower surface of plate and initial calm water surface; it is also the pitch angle of plate. Initially, the plate with an initial deadrise angle β_0 is placed at a distance $h = 0.1W$ above the water surface, and then it is released at a given velocity and accelerates downwards under gravity to the maximum velocity, which is defined as the impact velocity V_0. The gravity acceleration is set as $g = -9.81 \, \text{m/s}^2$.

Five initial deadrise angles β_0 are adopted: 0°, which represents a symmetrical air entrapment behavior for comparison; 1° to 3° of typical small deadrise angle range with air cushioning effect [15]; and 4°, where the air cushioning effect is very weak. For every initial deadrise angle, the impact velocity V_0 ranging from 1 to 7 m/s [23] are considered, as shown in Table I, where the three dimensionless parameters, namely, the Froude number Fr $= V_0/\sqrt{gW}$, Reynolds number Re $= \rho V_0 W/\mu$, and Weber number We $= \rho V_0^2 W/\sigma$ based on the water properties, impact velocity, and plate width are also given. The range of Froude number spans from 0.45 to 3.16, the magnitude of Reynolds number and Weber number are, respectively, on the order of 10^6 and 10^4, suggesting that the gravity plays an important role, while the global influence of viscosity and surface tension are insignificant.

For the atmosphere boundary, the velocity is set to a mixed condition pressureInletOutletVelocity, and the pressure is set to a totalPressure. The wall boundaries are set as no-slip wall condition. The plate is set as no-slip moving wall.

The multiblock structured mesh is generated using ANSYS ICEM 19.0, as shown in Fig. 2(b). Uniform mesh is applied in the near field surrounding plate and water surface. A grid- (time-step) independence study is conducted in the case of $V_0 = 1.5$ m/s and $\beta_0 = 1°$ by comparing the motion history of plate, which is the primary focus of this paper. First, a grid-independence study is performed to identify the suitable mesh resolution, as shown in Fig. 3(a). Three grids are created with variations in uniform-mesh region, including a coarse grid with $\Delta x = \Delta y = 1.5$ mm, a medium grid with $\Delta x = \Delta y = 1$ mm, and a fine grid with $\Delta x = \Delta y = 0.75$ mm, corresponding to the total cell number of 750 000, 1 500 000, and 3 000 000, respectively. The results of medium and fine grids coincide very well in the x_{CG}, y_{CG}, and β curves; hence, the medium grid is adopted. Second, a time-step independence study is performed based on the medium grid, as shown in Fig. 3(b). Three time steps including $\Delta t = 2 \times 10^{-5}$ s, 1×10^{-5} s, and 5×10^{-6} s are employed. Based on the results, the $\Delta t = 1 \times 10^{-5}$ s is adopted for further simulations. With the selected grid- (time-step) resolution, simulating a 2D water entry case with duration of 0.08 s costs approximately 1120 core hours using two Inter Xeon Gold 5218R CPUs (20 core, 2.1 GHz). The current study involves more than 40 simulation cases and would not have been feasible to be done in full 3D form, and therefore the 2D investigation is employed.

C. Validation of numerical method

The experiment performed by Ma *et al.* [19] at $\beta_0 = 0°$ and $V_0 = 5.5$ m/s is chosen to validate the present numerical method. In their experiment, a rigid flat plate of 32 kg was dropped freely to impact water. The plate was 0.25 m long, 0.25 m wide, and 0.012 m thick. Five miniature pressure probes were installed on the plate lower surface, one in the center and four at 15 mm distance from plate edges [see $P1$–$P5$ in Fig. 4(a)], to record the impact pressure.
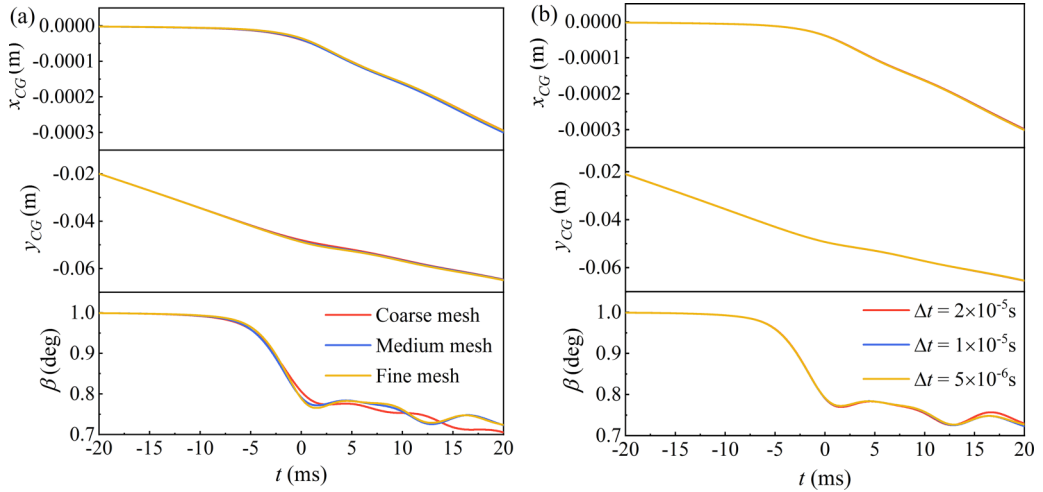
FIG. 3. Motion history of plate at $V_0 = 1.5$ m/s and $\beta_0 = 1°$ for (a) grid-independence study and (b) time-step independence study.
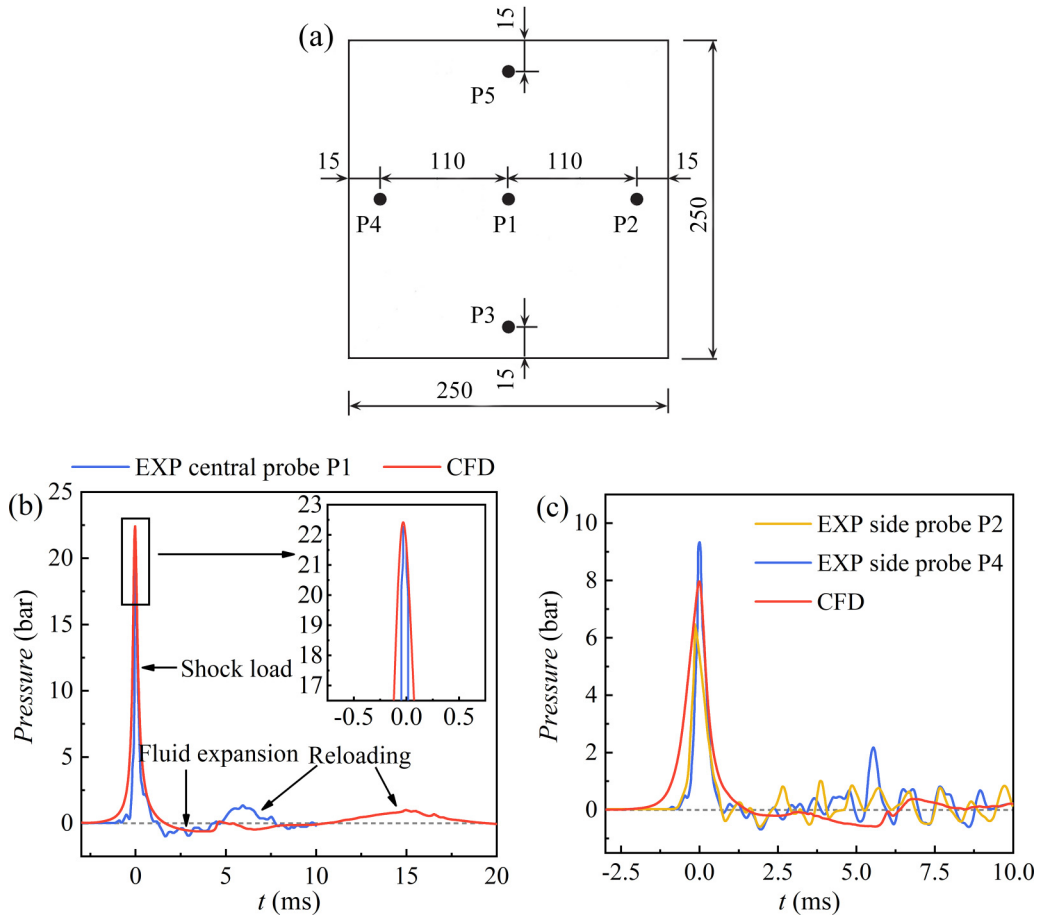

FIG. 4. (a) Schematic of pressure probes on plate lower surface (units in mm) [19], and time histories of gauge pressure at (b) central probe and (c) side probe.
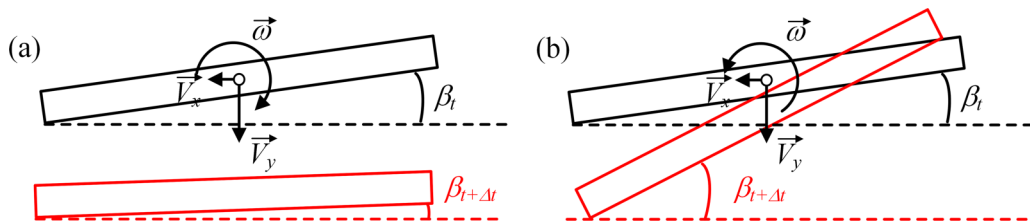
FIG. 5. Schematic of plate motions: (a) pitching down; (b) pitching up.

In the present 2D simulation, the plate size is set as 0.25 m in width and 0.012 m in height; the mass of plate per unit area is set as 512 kg/m^2 to be consistent with experimental setup. The 2D method is proven to be acceptable in capturing the peak pressure [32] and evolution process of impact load [33] of 3D results.

Ma *et al.* [19] observed that the impact pressure evolution has three distinct stages: shock load, fluid-expansion induced low subatmospheric pressure, and weaker reloading, as shown in Fig. 4(b), where the phases of pressure have been shifted to correlate the first peak to time $t = 0$ ms. The entire impact process is well simulated by the present numerical method. For the central probe, the simulated pressure peak at shock load stage agrees well with experimental result, while the time span for fluid expansion and reloading stages are longer than the experiment. This discrepancy can be explained by that the 2D setup makes it more difficult for the trapped air to escape compared to the 3D condition in the experiment, which, in turn, increases the rising and falling time in the impact pressure. The longer-duration phenomenon is also observed in the 2D numerical study by Aghaei *et al.* [33]. For the side probes, the experimental data at symmetric positions exhibit large scatters [Fig. 4(c)] due to water-surface disturbances or other practical issues in the experiment. The calculated pressure peak is very close to the averaged value of $P2$ and $P4$, and the pressure evolution has generally fair agreement with experimental results. Overall, apart from the longer duration of fluid expansion and reloading stage due to 2D setup, the present numerical method has shown promising ability in capturing impact load and typical physical stages during the water impact process.

III. RESULTS AND DISCUSSION

A. Plate motion response induced by air cushioning effect

Figure 5 sketches the motions of plate during water impact process, and Fig. 6 depicts the motion history at different impact velocities and initial deadrise angles. Throughout the paper, the impact time $t = 0$ ms is defined as the time when the first peak of vertical impact force coefficient in Eq. (5) occurs.

For $\beta_0 = 0°$ [Fig. 6(a)], during the whole impact process, the plate only experiences the vertical translation. The shift of CG in the horizontal direction is on the order of 1×10^{-5} m, and the maximum change of pitch angle is less than $0.08°$. Hence, both the horizontal translational motion and pitching motion due to tiny asymmetries in the flow behavior are negligible.

For $\beta_0 > 0°$ the motions of plate are much more varied and complicated. After being released, the plate accelerates downwards and slightly pitches down before the impact time. At $t = 0$ ms, the impact occurs and greatly affects the subsequent motion behavior, and an obvious inflection point can be observed on all the motion curves. In the horizontal direction, the translational motion is triggered so that the plate begins to move toward left (the keel direction) but very slowly; in the vertical direction, the descending velocity decreases suddenly, as can be judged from a sudden change in the slope of y_{CG} curve. Generally, the higher the impact velocity is, the greater is the change in translational motion but following the same trend, while the pitching motion exhibits significant differences when the impact condition is different, which can be classified into four
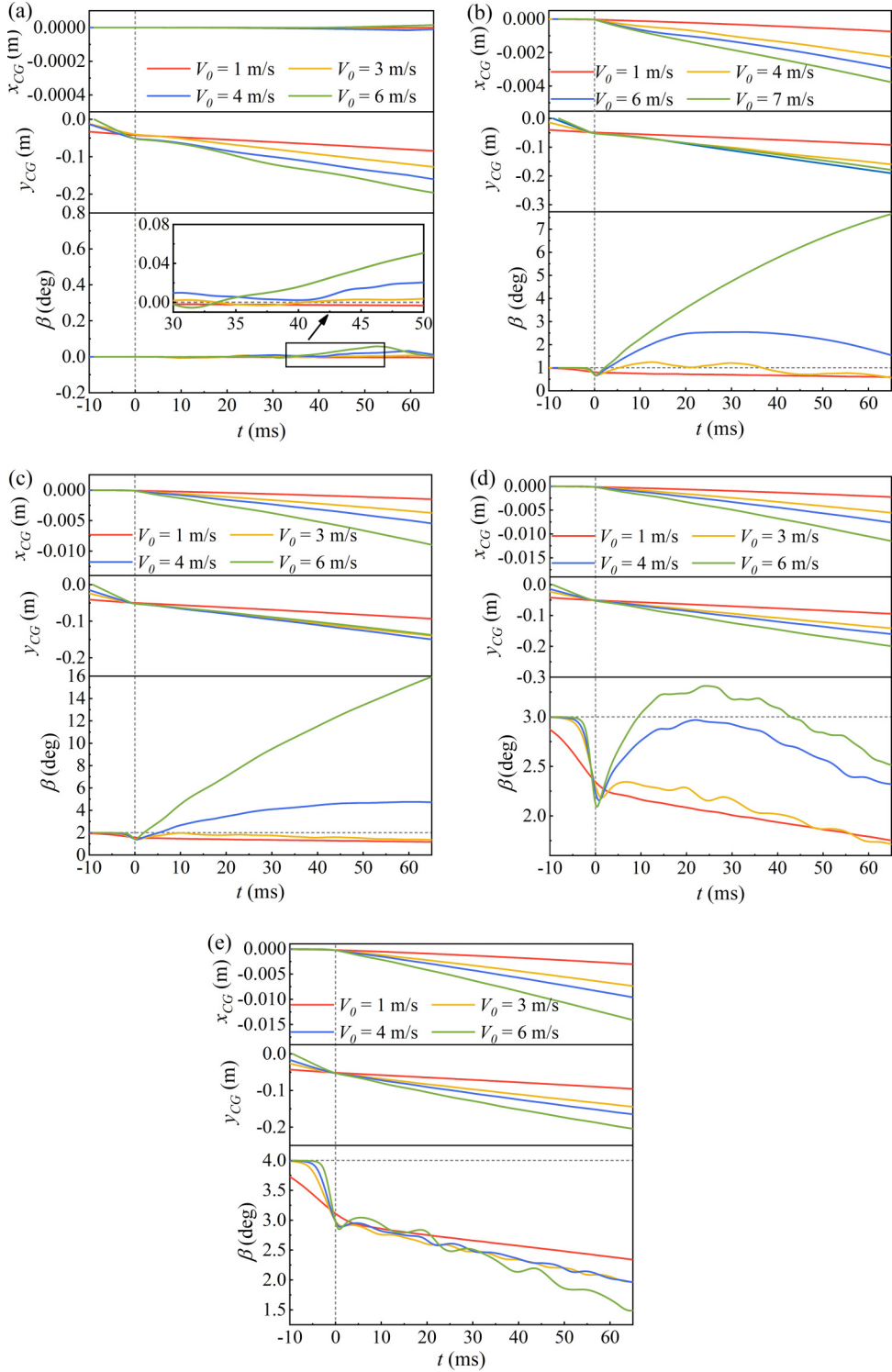
FIG. 6. Motion history of plate at different impact velocities for (a) $\beta_0 = 0°$, (b) $\beta_0 = 1°$, (c) $\beta_0 = 2°$, (d) $\beta_0 = 3°$, and (e) $\beta_0 = 4°$.
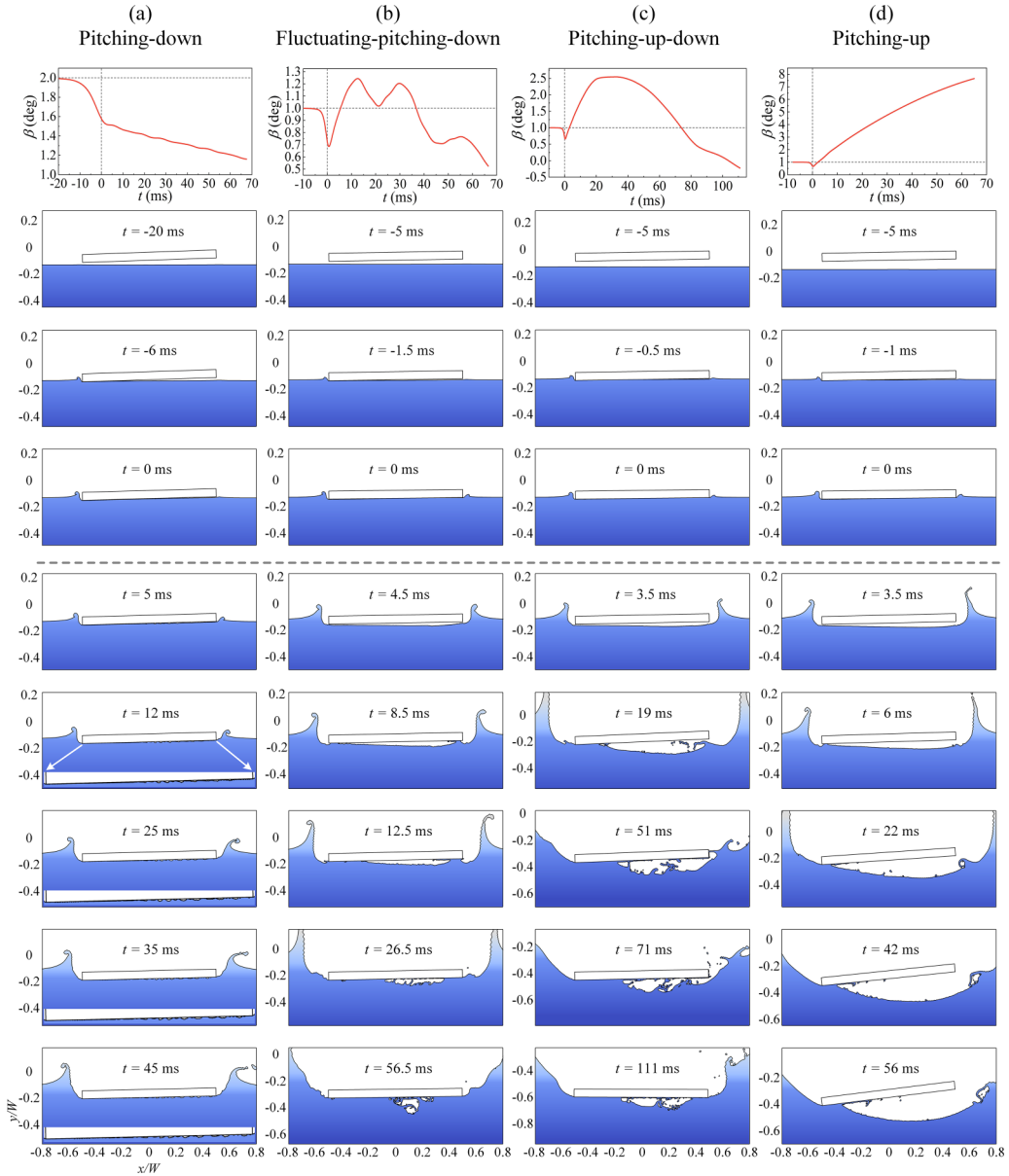
FIG. 7. Water-air interface (identified by $\alpha_{water} = 0.5$) for characteristic motion patterns: (a) pitching-down at $V_0 = 1$ m/s and $\beta_0 = 2°$, (b) fluctuating–pitching-down at $V_0 = 4$ m/s and $\beta_0 = 1°$, (c) pitching-up–down at $V_0 = 6$ m/s and $\beta_0 = 1°$, and (d) pitching-up at $V_0 = 7$ m/s and $\beta_0 = 1°$.

characteristic patterns in general based on the variation history of pitch angle after impact ($t > 0$ ms): pitching-down, fluctuating-pitching-down, pitching-up-down, and pitching-up, as shown in Fig. 7, which is an interesting phenomenon to be noted. At a given time, the instantaneous pitching down refers to the plate rotating clockwise and the pitch angle decreasing, and the instantaneous pitching up refers to the opposite, as sketched in Fig. 5.

The pitching-down motion refers to a pattern where the pitch angle decreases monotonically throughout the whole impact process [Fig. 7(a)]. During this water entry process, the plate keel
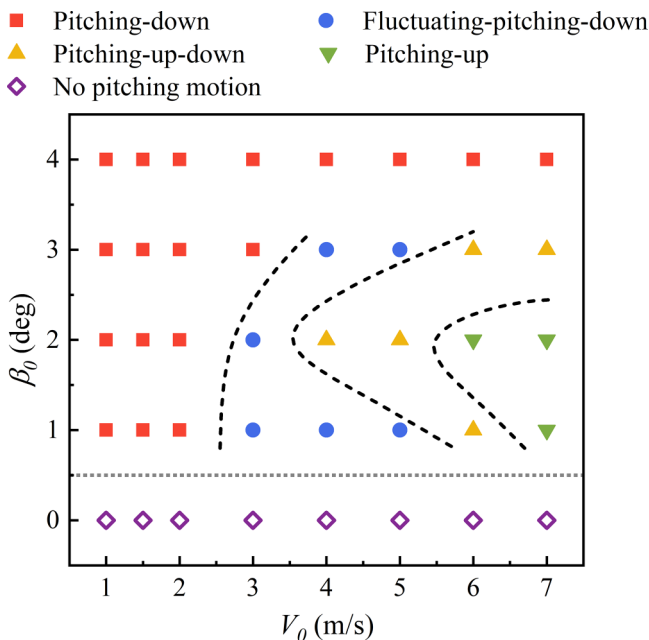
FIG. 8. Regime map of motion patterns according to V_0-β_0.

first contacts water; then the entire plate slowly pitches down to lie on water surface. It can be observed that several air bubbles are entrapped under plate edge, consistent with observations by Bagg *et al.* [16].

In the fluctuating–pitching-down motion, the plate first pitches up, during which the pitch angle increases to its maximum, and then pitches down accompanied by fluctuations [Fig. 7(b)]. In this process, the plate edge is always attached to water surface, which encloses a large air bubble beneath plate; hence, there are fluctuations in the pitch-angle curve due to compression-expansion behavior of trapped air bubble.

The pitching-up–down-motion pattern is a combination of a monotonical pitching up and a following monotonical pitching down [Fig. 7(c)]. For this case, the pitching up motion is much stronger and the plate edge is detached from water surface for a short period [$t = 19$ ms of Fig. 7(c)]; then, it pitches down monotonically until plate edge reattaches with water surface [$t = 111$ ms of Fig. 7(c)].

The pitching-up motion refers to a pattern where the pitch angle increases monotonically during the water entry process [Fig. 7(d)]. For this pattern, the pitching up motion is very striking and durable. The increase in pitch angle is significant, approaching $7.5°$ for the case of $V_0 = 7$ m/s and $\beta_0 = 1°$ [Fig. 6(b)] and $16°$ for the case of $V_0 = 6$ m/s and $\beta_0 = 2°$ [Fig. 6(c)]. It appears that the plate edge is bounced up violently by the air layer.

In this paper, for most cases, the simulation time after impact is 65 ms. For the pitching-up–down cases, e.g., the case of $V_0 = 6$ m/s and $\beta_0 = 1°$ in Fig. 7(c), the simulation time is elongated to observe that the plate edge reattaches with water surface. In this paper, the aforementioned pitching-motion patterns are identified based on the motion history during postimpact 65 ms.

Figure 8 depicts the regime map of four motion patterns. For $\beta_0 = 0°$, there is no pitching motion observed; for $\beta_0 > 0°$, four regimes exist: pitching-down, fluctuating-pitching-down, pitching-up-down, and pitching-up, as separated by three black dashed lines. This phenomenon preliminarily indicates the distinct difference in air cushioning effect between zero and small initial deadrise angles. The pitching-down motion mainly occurs for low V_0 and large β_0; conversely, the pitching-up

motion occurs only for high V_0 and very small β_0 ($V_0 \geqslant 6$ m/s and $\beta_0 \leqslant 2°$). The fluctuating–pitching-down and pitching-up–down motions exist in between.

B. General impact process at small initial deadrise angles

Before investigating the physics accounting for different motion patterns, the water impact process of flat plate at small initial deadrise angles needs to be well understood. In this part, the evolution of flow physics and impact force throughout the whole impact process will be analyzed in detail, particularly, the compression-expansion process of trapped air. The simulated results show that all the cases have similar four physical stages and compression-expansion behaviors of trapped air; thus, this section just takes the result of $V_0 = 4$ m/s and $\beta_0 = 1°$ as an example to reveal the general impact process.

For convenience in explaining results, the following impact force coefficients are introduced. The horizontal force coefficient, vertical force coefficient, pitching-moment coefficient, and pressure coefficient are defined as

$$C_x = \frac{F_x}{1/2 \rho_{\text{water}} V_0^2 W}, \tag{4}$$

$$C_y = \frac{F_y}{1/2 \rho_{\text{water}} V_0^2 W}, \tag{5}$$

$$C_m = \frac{M}{1/2 \rho_{\text{water}} V_0^2 W^2}, \tag{6}$$

$$C_p = \frac{p - p_\infty}{1/2 \rho_{\text{water}} V_0^2}, \tag{7}$$

where F_x and F_y are, respectively, the horizontal and vertical component of resultant impact force on the plate per unit length (the length orientation is perpendicular to the page), M is the pitching moment about CG per unit length, p is the pressure, and $p_\infty = 101325$ Pa is the pressure of surrounding quiescent air.

1. Flow physics

During the falling process, the plate bottom and the water surface form a channel. The compression-expansion process of air can be qualitatively understood by the variations in this channel geometry and flow behavior inside. Figure 9(b) extracts the variations of channel height at three stations along the plate-width direction, as sketched in Fig. 9(a): $x/W = -0.4$ close to plate keel, $x/W = 0$ at plate center, and $x/W = 0.4$ close to plate edge. Correspondingly, Fig. 9(c) depicts the position variations of plate bottom and water surface in the global coordinate system. Figure 10 extracts velocity profiles at several positions in the channel, and Fig. 11 depicts the pressure coefficient distribution on plate lower surface, correspondingly.

From being released to the time of $t = -5.0$ ms, the plate constantly moves downwards, while the water surface keeps quiescent persistently under great inertia, as shown in Fig. 9(c). During this process, the air escapes freely from both gaps under plate keel and plate edge [Fig. 10(a)], and the pressure coefficient on plate bottom is almost zero [Fig. 11(a)]. In Fig. 10(a), it can be noted that the water surface under plate center slightly deforms downward and the water surface under plate keel and edge slightly rises prior to impact, which is caused by the air cushioning. The stagnant air flow under the plate center and the high-speed air flow under the plate keel and edge, respectively, exerts pressure and suction on local water surface.

As the plate descends further to about the time of $t = -1.5$ ms, the water surface is further disturbed, and the channel height under the plate keel ($x/W = -0.4$) decreases to the minimum value approaching 0 [Figs. 9(b) and 9(c)], and a water jet is formed outside plate keel [Figs. 10(b) and 10(c)]. During this process, the gap under plate keel is very small and is blocked by the water jet, so almost no air can escape from the keel side; the gap under plate edge is much broader, so
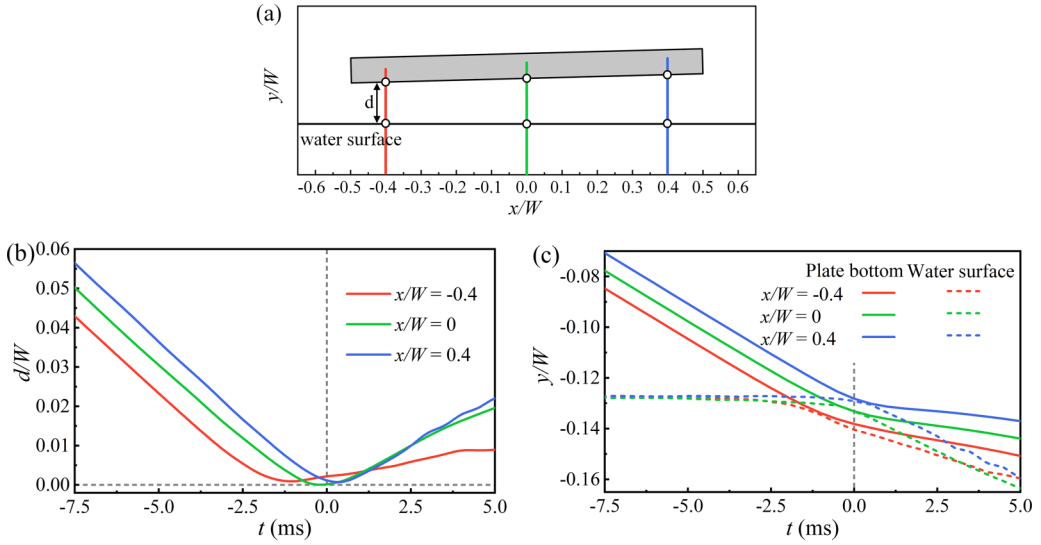
FIG. 9. (a) Schematic of three stations in the plate width direction: $x/W = -0.4$, 0, and 0.4. (b) Height variations of the channel between plate bottom and water surface. (c) Vertical position variations of plate bottom and water surface in the global coordinate system at $V_0 = 4$ m/s and $\beta_0 = 1°$.

the air mainly escapes from this side, like a rapidly propagating air jet. The closer to the plate edge, the higher the air flow velocity is, and the maximum velocity even approaches to 200 m/s, which is consistent with observations by Abrahamsen *et al.* [24]. Due to the shrinking air-escaping gap under plate keel, the air under the keel area is compressed by descending plate and the pressure increases,
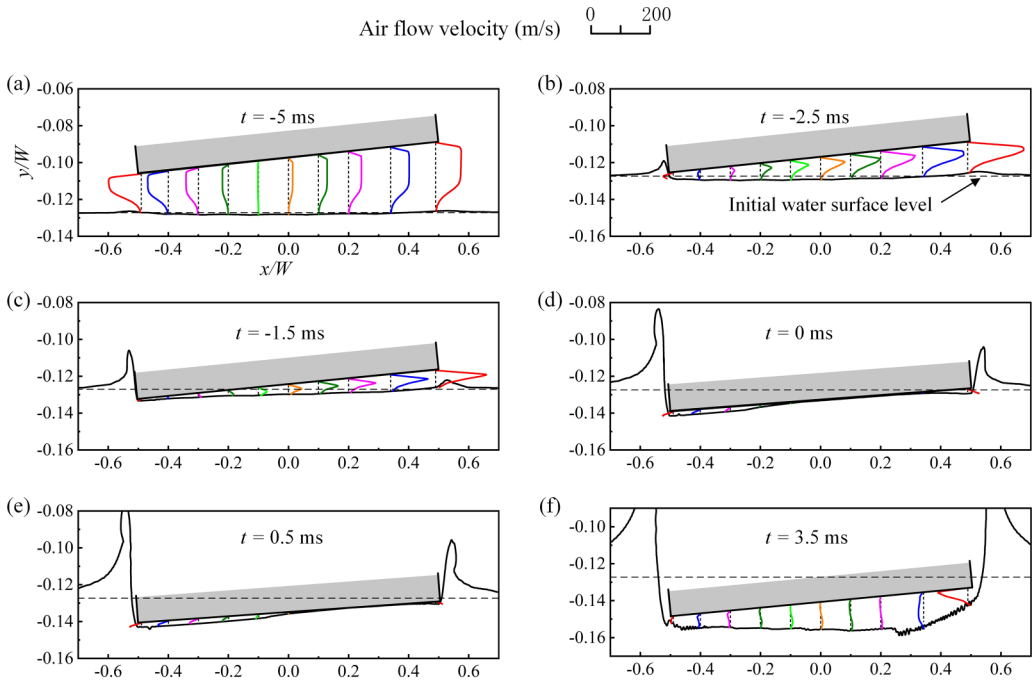

FIG. 10. Velocity profiles of air in the channel between plate bottom and water surface at $V_0 = 4$ m/s and $\beta_0 = 1°$; only the plate bottom is shown for brevity.
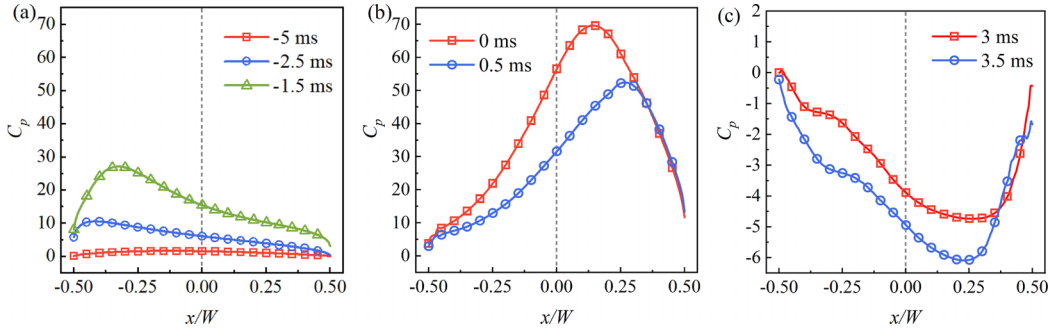
FIG. 11. Pressure coefficient distribution on plate lower surface for (a) keel compression, (b) edge compression, and (c) fluid expansion stage at $V_0 = 4$ m/s and $\beta_0 = 1°$.

which is like a moving piston. The highest pressure is located at plate keel and gradually decreases toward plate edge, as shown in Fig. 11(a), exerting a pitching-down moment about CG. This stage is called the keel compression in this paper.

As the water entry continues to the impact time of $t = 0.5$ ms, the water surface under plate keel is pushed downwards slowly by the local high air pressure, while the water surface under plate edge still stays quiescent [Fig. 10(d) and 10(e)]. Thus, the channel height under plate keel ($x/W = -0.4$) begins to increase slowly while the height under plate edge ($x/W = 0.4$) continually decreases to the minimum value approaching 0 [Figs. 9(b) and 9(c)]. During this process, the air beneath plate edge begins to get heavily compressed, which leads to a significant increase in the pressure coefficient near plate edge, as shown in Fig. 11(b), and results in a pitching-up moment about CG. This stage is called the edge compression in this paper. Compared to the keel compression, the edge compression is much stronger judged from the magnitude of impact pressure. This is because at latter stage, both the air-escaping gaps under plate keel and plate edge are very small, and therefore the air is compressed more significantly.

Thereafter, the high air pressure in the channel forces the plate to decelerate and the water surface to accelerate downwards [Fig. 9(c)], where the water below plate is displaced downwards and outwards quickly, to be finally injected into the water jet. During this stage, the space of channel between plate bottom and water surface quickly increases [Fig. 9(b)], and the air-flow velocity in the channel is very small [Fig. 10(f)]. Consequently, the compressed air inside expands and the pressure coefficient decreases even to negative value, as shown in Fig. 11(c), and the pressure under plate edge is obviously smaller than that under plate keel due to larger local channel height, exerting a pitching-down moment about CG. This stage is called the fluid expansion in this paper.

As the plate penetrates further, the air flow ceases, because the plate bottom directly contacts the deformed water surface along its periphery and encloses the air layer into an air bubble, as depicted in Fig. 12. After that, the air bubble repeats the compression [see Figs. 12(a) to 12(c)] and expansion [see Figs. 12(c) to 12(e)] process, causing the local pressure to oscillate periodically, and produces secondary impact load on the plate but is considerably weak, e.g., the trough and peak of pressure coefficient ranges merely from -2.5 to 3.75. This process is called the reloading stage in this paper.

2. Impact force

Figure 13 shows the time histories of C_x, C_y, and C_m. The evolution of C_y maintains the similarity with zero-deadrise angle condition in exhibiting three distinct stages: a high peak load due to air compression; a negative impact force due to fluid expansion; and less severe secondary impact forces due to periodic compression-expansion behavior of air bubble. Following definitions of Ma *et al.* [19] in zero-deadrise angle condition, they are, respectively, termed as shock load stage (the white-background part), fluid expansion stage (the gray-background part), and reloading stage (the
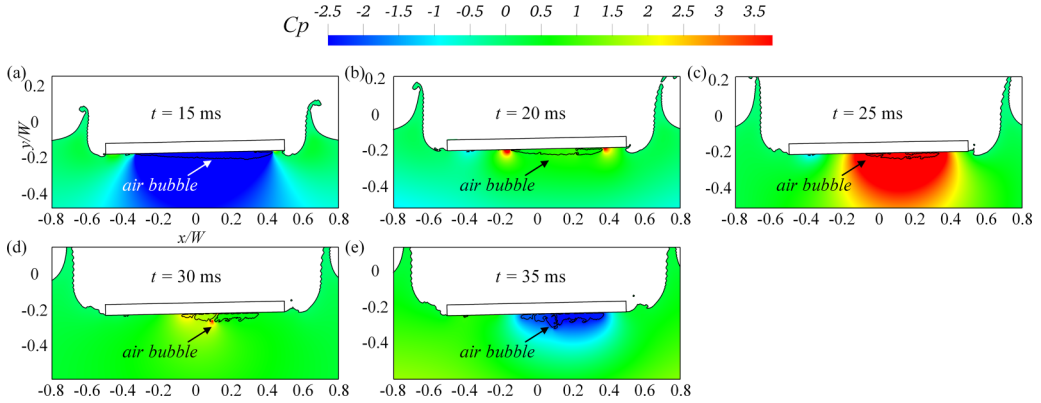
FIG. 12. Water-air interface and pressure contour for reloading stage at $V_0 = 4$ m/s and $\beta_0 = 1°$.

blue-background part). For $\beta_0 > 0°$, C_x is proportional to C_y, because they are mainly orthogonal components of impact pressure on the plate where the viscous effects are insignificant [19], and triggers the horizontal translational motion in Fig. 6. For the C_m curve, there are two prominent pitching moments observed at shock load stage: a pitching-down moment (marked in orange) due to keel compression, and a subsequent pitching-up moment (marked in green) due to edge compression. Compared with the pitching-down moment, the maximum of pitching-up moment is higher but the duration is slightly shorter. Thus, the shock load stage is further divided into two substages: keel compression stage and edge compression stage, as divided by the blue-dashed line. At fluid expansion stage, the plate experiences a weak pitching-down moment, followed by weak oscillating moments at reloading stage.
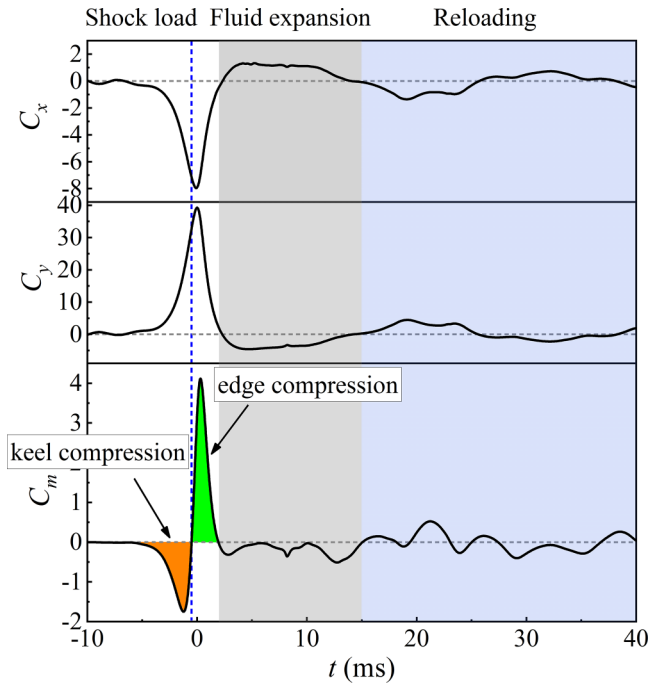

FIG. 13. Time histories of horizontal force coefficient, vertical force coefficient, and pitching-moment coefficient at $V_0 = 4$ m/s and $\beta_0 = 1°$.
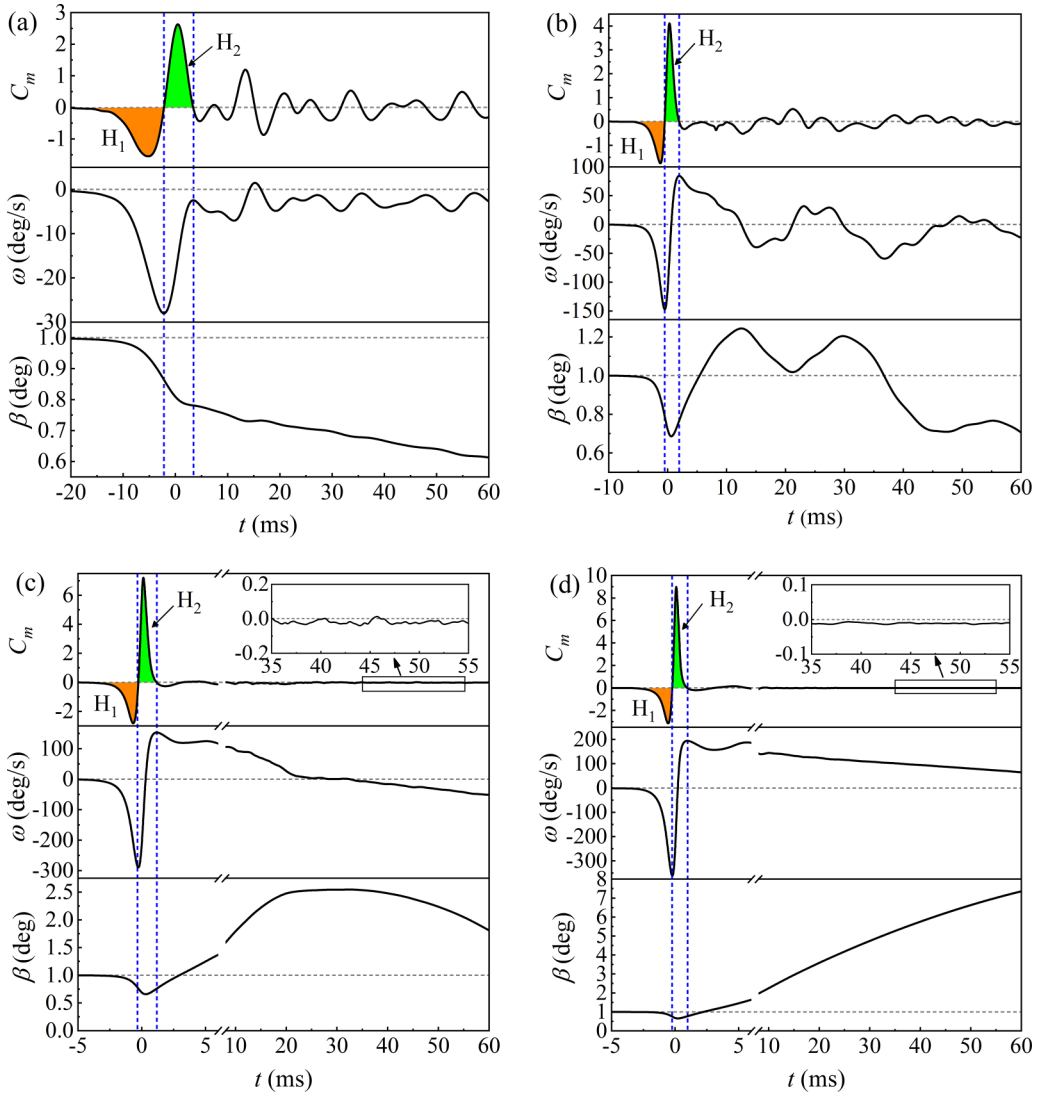
FIG. 14. Time histories of pitching-moment coefficient, angular velocity, and pitch angle at $\beta_0 = 1°$ for (a) $V_0 = 1$ m/s, (b) $V_0 = 4$ m/s, (c) $V_0 = 6$ m/s, and (d) $V_0 = 7$ m/s.

C. Physics of different motion patterns

In this part, the relation between the four pitching-motion patterns and the aforementioned pitching moments, particularly, those behind physical processes, will be investigated. The analysis is performed under different impact velocities and initial deadrise angles to illustrate the influence of impact condition on the pitching-motion patterns.

1. Influence of impact velocity on pitching motion

Figure 14 depicts the time histories of pitching-moment coefficient, angular velocity, and pitch angle at different impact velocities of a fixed initial deadrise angle $\beta_0 = 1°$. The moment of impulse is introduced to evaluate how significantly each impact stage affects the pitching motion of plate,
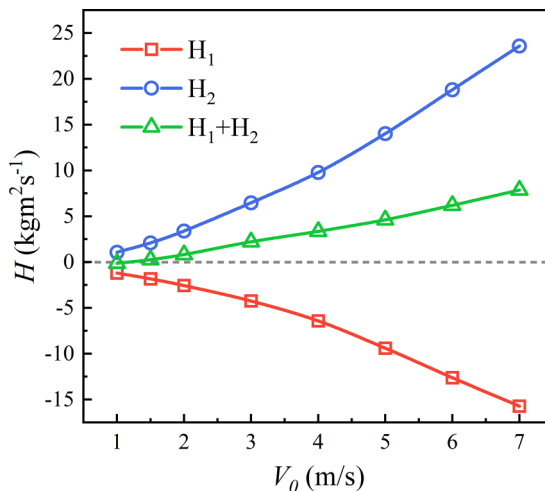
FIG. 15. Moment of impulse for keel compression stage and edge compression stage at different impact velocities, $\beta_0 = 1°$.

which is defined as

$$H = \int_{t_i}^{t_f} M(t)dt, \tag{8}$$

where t_i and t_f are the start and final times for a certain physical stage. The two prominent moments of impulse for keel compression and edge compression stages are found to be essential in determining the motion behavior of plate; they are, respectively, denoted by H_1 and H_2 in this paper, as given in Fig. 15. Where the H_1 is negative and acts to facilitate the pitching down, the H_2 is positive and promotes the pitching up; the sum of $H_1 + H_2$ represents their combined effects. When the impact velocity increases, the keel and edge compressions are enhanced but not to the same extent, and the sum of $H_1 + H_2$ gradually increases from a very small negative value to a positive one, i.e., the pitching motion evolves from pitching down into pitching up.

At low impact velocity of $V_0 = 1$ m/s [Fig. 14(a)], the plate performs pitching-down motion. As the plate approaches water surface, it first experiences a pitching-down moment due to keel compression (the negative H_1). Correspondingly, the angular velocity ω gradually decreases and achieves its minimum by the end of keel compression stage, and the pitch-angle β gradually decreases. Then, the edge compression occurs and the plate experiences a pitching-up moment (the positive H_2), which causes ω to increase but is still negative by the end of edge compression stage. Hence, the plate continues to pitch down but at a much lower angular velocity. The physical reason can be explained: at low impact velocity, the intensity of keel compression is slightly stronger than edge compression, judged from the impulse value of pitching moment in Fig. 15; thus, the H_1 overwhelms H_2 and causes ω to be negative at the end of edge compression stage. Thereafter, the plate experiences a weak pitching moment with low-amplitude oscillation due to the fluid expansion and the periodic compression-expansion behavior of many small air bubbles, and the ω always stays negative. Thus, the plate pitches down monotonously during the whole impact process.

At the impact velocity of $V_0 = 4$ m/s [Fig. 14(b)], the plate undergoes fluctuating–pitching-down motion. For this case, after the initial pitch down due to H_1, the negative ω quickly increases and finally to a positive value by the end of edge compression stage due to the greater H_2. Hence, the plate pitches up and the pitch angle β gradually increases. After that, the weak pitching-down
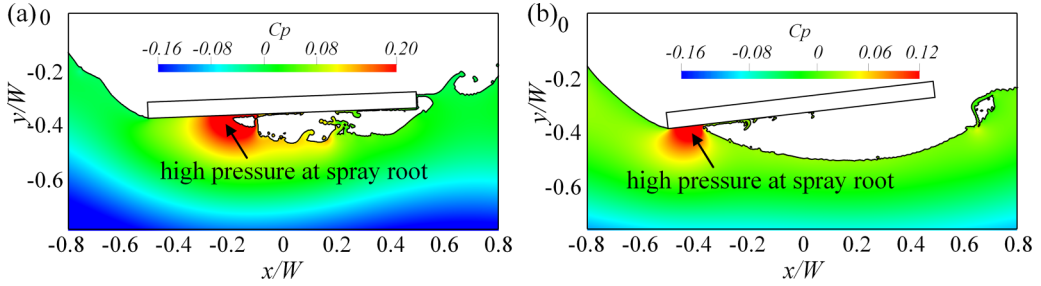
FIG. 16. Water-air interface and pressure contour when the plate edge detaches from water surface at $\beta_0 = 1°$ for (a) $t = 51$ ms of $V_0 = 6$ m/s and (b) $t = 50$ ms of $V_0 = 7$ m/s.

moment due to fluid expansion causes ω to decrease and fall back to negative value again, which makes the plate pitch down. The pitching down process is combined with fluctuations, because the pitching up motion is not strong enough to enable the plate edge to detach from water surface and there is still a large air bubble entrapped [Fig. 7(b)].

At the impact velocity of $V_0 = 6$ m/s [Fig. 14(c), where the t axis is broken for clarity], the plate performs pitching-up–down motion. For this case, the pitching up motion due to edge compression is very strong. The increase in pitch angle is so significant that the plate edge finally detaches from water surface [Fig. 7(c)]. There is no air bubble entrapped, and therefore, there is no fluctuation on the pitch-angle curve. An interesting phenomenon should be noted: when the plate keel is immersed in water while plate edge is not, the plate would be subject to additional pitching-down moments [zoomed-in area of Fig. 14(c)] contributed by the high pressure in the water spray-root region near plate keel, as indicated by the black arrow in Fig. 16. Consequently, the ω constantly decreases, and when it decreases to negative value, the plate starts to pitch down until plate edge reattaches with water surface. The overall motion history exhibits a durable pitching-up–down pattern.

At the high impact velocity of $V_0 = 7$ m/s [Fig. 14(d)], the plate conducts pitching-up motion, because the edge compression process becomes extremely strong and completely dominates the pitching motion. The pitching up motion is extremely significant; visually, it appears that the plate edge is bounced up violently [Fig. 7(d)]. The pitching up motion is also very durable. The highest angular velocity is close to 200 deg/s; thus, it requires a large amount of time to decay to zero under weak pitching-down moments due to high pressure in the spray root region, as shown in Fig. 16. And, it can be speculated that if the simulation time is sufficiently long, the plate would finally pitch down.

2. Influence of initial deadrise angle on pitching motion

To elucidate the influence of initial deadrise angle on pitching motion, Fig. 17 compares the time histories of pitching-moment coefficient, angular velocity, and pitch angle at different initial deadrise angles of a fixed impact velocity $V_0 = 4$ m/s, and Fig. 18 depicts the corresponding evolution processes of water-air interface. The case of $\beta_0 = 3°$ is not shown for brevity, because it exhibits the same motion pattern with $\beta_0 = 1°$. It is noted the cases illustrated here are different from Fig. 7 to avoid confusion.

For $\beta_0 = 0°$, the trapped air bubble is located under plate center and presents a high symmetry [Fig. 18(a)]. Hence, during the whole impact process, the magnitude of pitching moment is very small and oscillates randomly due to tiny asymmetries in the flow behavior. The variations of pitch angle are within $0.03°$; thus, the pitching motion due to air cushioning effect is negligible.
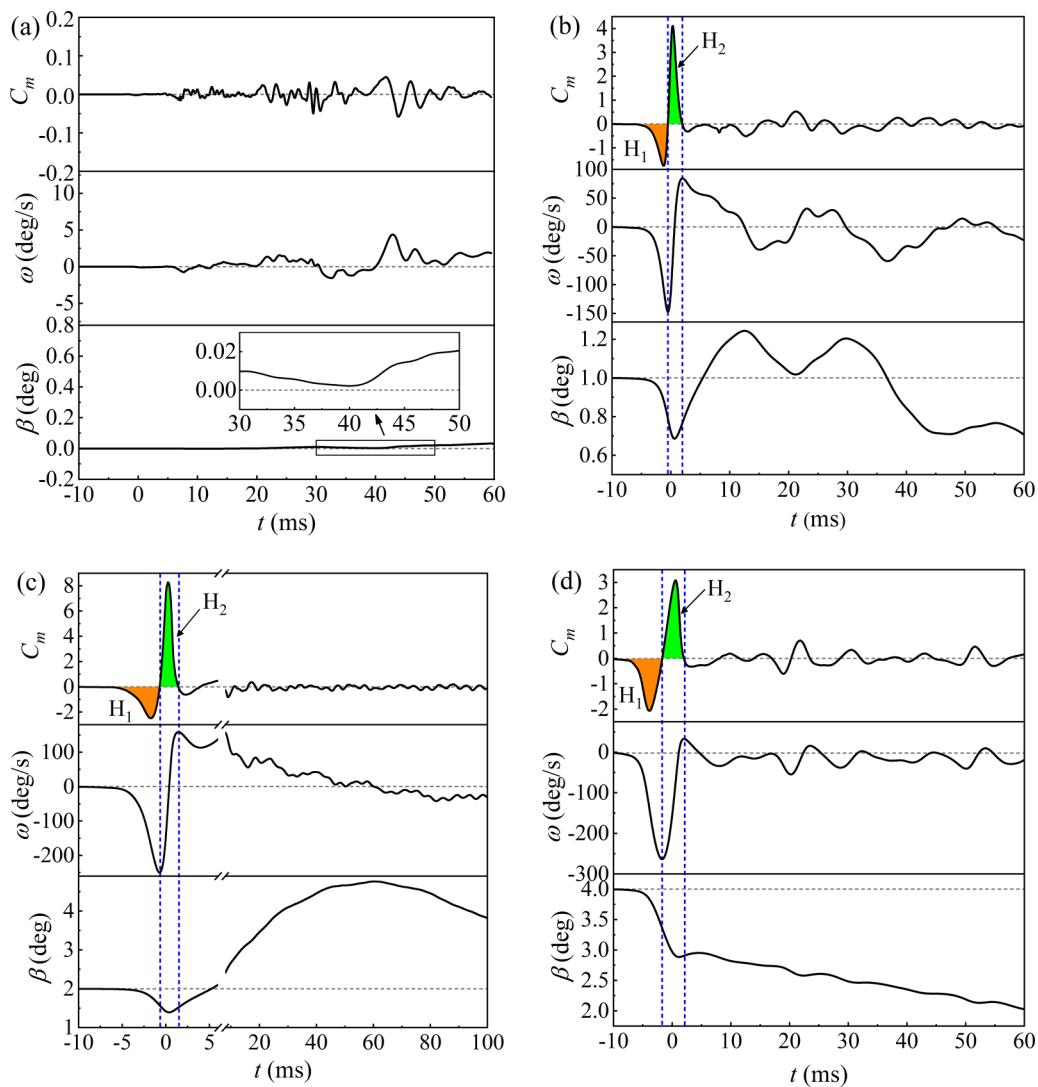
FIG. 17. Time histories of pitching moment coefficient, angular velocity, and pitch angle at $V_0 = 4$ m/s for (a) $\beta_0 = 0°$, (b) $\beta_0 = 1°$, (c) $\beta_0 = 2°$, and (d) $\beta_0 = 4°$.

For $\beta_0 > 0°$, the trapped air is very asymmetrical about plate center; thus, the pitching motion due to air cushioning effect becomes noticeably stronger immediately. As shown in Fig. 19, when the initial deadrise angle increases from $\beta_0 = 1°$ to $4°$, the negative H_1 first decreases and then tends to a constant; the positive H_2 first increases and then decreases, with the maximum value at $\beta_0 = 2°$. The resulting $H_1 + H_2$ is positive due to the domination of edge compression, and varies in the same trend with H_2. Correspondingly, the pitching-up trend first enhances and then weakens with the increasing β_0, where the most violent pitching motion due to air cushioning effect occurs at $\beta_0 = 2°$. This variation trend is also observed at other impact velocities, e.g., $V_0 = 5$ m/s (Fig. 8), and is qualitatively consistent with the conclusion of Okada and Sumi [15] that the maximum impact pressure for water impact of plate occurs at $\beta_0 = 2° \sim 3°$. For $\beta_0 = 4°$, where the air cushioning effect is very weak, the plate performs pitching-down motion regardless of impact velocity (Fig. 8), because most air escapes and there is barely no air entrapped [Fig. 18(d)].
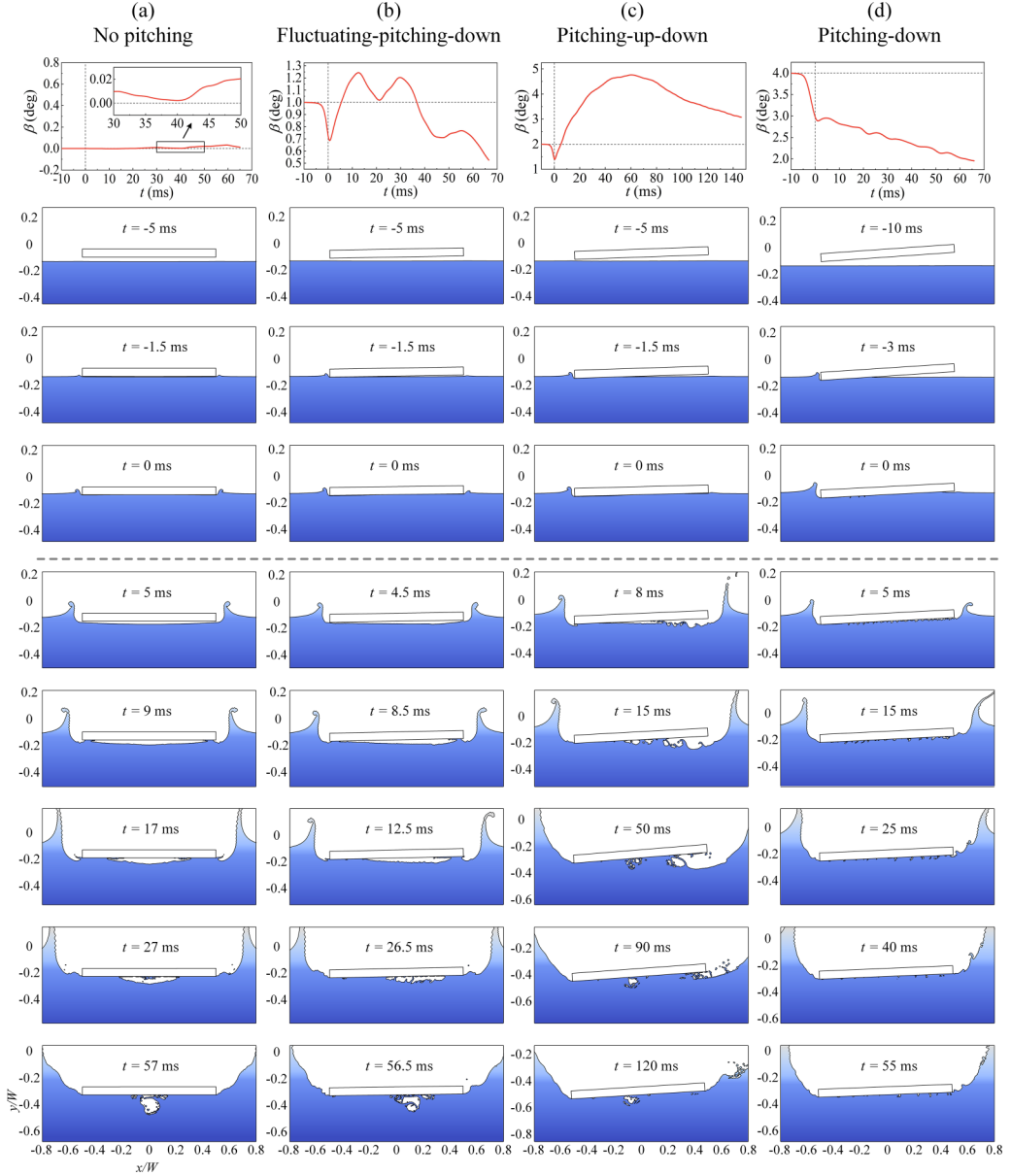
FIG. 18. Water-air interface (identified by $\alpha_{water} = 0.5$) at $V_0 = 4$ m/s for (a) $\beta_0 = 0°$, (b) $\beta_0 = 1°$, (c) $\beta_0 = 2°$, and (d) $\beta_0 = 4°$.

IV. CONCLUSIONS

When a flat plate falls freely to impact water at small initial deadrise angles, the air cushioning effect under plate bottom is asymmetrical about plate center and produces great asymmetrical impact pressure. In this paper, the motion response of plate in such an occasion was systematically studied. Major discoveries and conclusions are as follows:

In the regime of impact velocity and initial deadrise angle, four typical plate motion patterns have been discovered based on the variation characteristics of pitch angle: pitching–down, fluctuating-pitching-down, pitching-up-down, and pitching–up.
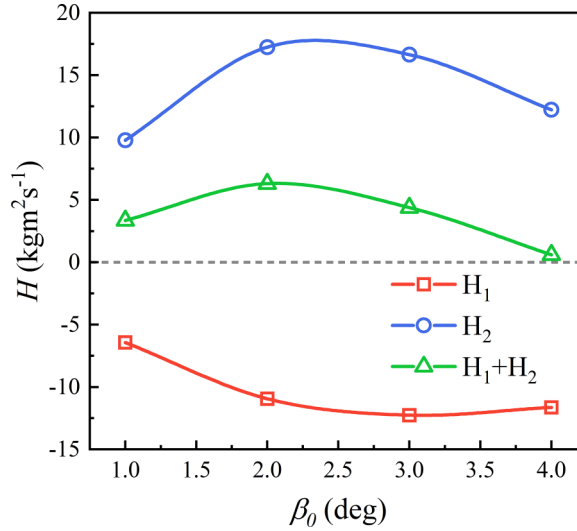
FIG. 19. Moment of impulse for keel compression stage and edge compression stage at different initial deadrise angles, $V_0 = 4$ m/s.

Based on the flow physics and impact forces on plate, the water impact process at small initial deadrise angles is divided into four distinct stages: keel compression, edge compression, fluid expansion, and reloading. The pitching-motion patterns are mainly determined by the keel compression and edge compression stages. In the keel compression stage, the air underneath plate keel is compressed and produces a pitching-down moment; in the following edge compression stage, the air underneath plate edge is heavily compressed and produces a strong pitching-up moment.

At low impact velocity, the keel compression dominates the motion behavior; thus, the plate performs pitching-down motion; with the increasing impact velocity, the edge compression quickly enhances and takes the dominant status; hence, the motion behavior gradually transits to fluctuating-pitching-down, pitching-up–down, and even pitching-up at high impact velocity. At zero initial deadrise angle, the air cushioning effect is symmetrical; thus, there is no pitching motion; with the increasing initial deadrise angle, the edge compression and its induced pitching up motion trend first enhance and then weaken; for the initial deadrise angle larger than $3°$, the air cushioning effect is very weak; thus, the plate only performs pitching-down motion.

[1] O. M. Faltinsen, M. Landrini, and M. Greco, Slamming in marine applications, J. Eng. Math. **48**, 187 (2004).

[2] T. Allen and M. Battley, Quantification of hydroelasticity in water impacts of flexible composite hull panels, Ocean Eng. **100**, 117 (2015).

[3] F. Dias and J. M. Ghidaglia, Slamming: Recent progress in the evaluation of impact pressures, Annu. Rev. Fluid Mech. **50**, 243 (2018).

[4] S. Abrate, Hull slamming, Appl. Mech. Rev. **64**, 60803 (2011).

[5] Y. L. Zheng, Q. L. Qu, P. Q. Liu, X. L. Wen, and Z. C. Zhang, Numerical analysis of the porpoising motion of a blended wing body aircraft during ditching, Aerosp. Sci. Technol. **119**, 107131 (2021).

[6] E.-M. Yettou, A. Desrochers, and Y. Champoux, Experimental study on the water impact of a symmetrical wedge, Fluid Dyn. Res. **38**, 47 (2006).

[7] L. Vincent, T. Xiao, D. Yohann, S. Jung, and E. Kanso, Dynamics of water entry, J. Fluid Mech. **846**, 508 (2018).

[8] Q. L. Qu, R. Wang, H. Guo, P. Q. Liu, and R. K. Agarwal, Numerical study of water impact of an elastic cylindrical shell, AIAA J. **54**, 3296 (2016).

[9] C. O. Ng and S. C. Kot, Computations of water impact on a two-dimensional flat-bottomed body with a volume-of-fluid method, Ocean Eng. **19**, 377 (1992).

[10] M. C. Lin and L. D. Shieh, Simultaneous measurements of water impact on a two-dimensional body, Fluid Dyn. Res. **19**, 125 (1997).

[11] H. Mayer and R. Krechetnikov, Flat plate impact on water, J. Fluid Mech. **850**, 1066 (2018).

[12] R. Krechetnikov, Physics of singularities in pressure-impulse theory, Phys. Rev. Fluids **3**, 054003 (2018).

[13] T. von Kármán, The impact on seaplane floats during landing, Report No. NACA-TN-321 (National Advisory Committee for Aeronautics, Washington, DC, 1929).

[14] H. Wagner, Über stoß- und gleitvorgänge an der oberfläche von flüssigkeiten, Z. Angew. Math. Mech. **12**, 193 (1932).

[15] S. Okada and Y. Sumi, On the water impact and elastic response of a flat plate at small impact angles, J. Mar. Sci. Technol. **5**, 31 (2000).

[16] J. Bagg, M. Pitto, and T. Allen, Quantification of spatial free-surface air entrapment during rigid body impacts into a quiescent fluid, Ocean Eng. **259**, 112060 (2022).

[17] F. J. Huera-Huarte, D. Jeon, and M. Gharib, Experimental investigation of water slamming loads on panels, Ocean Eng. **38**, 1347 (2011).

[18] S. L. Chuang, Experiments on slamming of wedge shaped bodies, J. Ship Res. **11**, 190 (1967).

[19] Z. H. Ma, D. M. Causon, C. G. Minghan, T. Mai, D. Greaves, and A. Raby, Pure and aerated water entry of a flat plate, Phys. Fluids **28**, 016104 (2016).

[20] U. Jain, P. Vega-Martínez, and D. van der Meer, Air entrapment and its effect on pressure impulses in the slamming of a flat disc on water, J. Fluid Mech. **928**, A31 (2021).

[21] U. Jain, A. Gauthier, D. Lohse, and D. van der Meer, Air-cushioning effect and kelvin-helmholtz instability before the samming of a disk on water, Phys. Rev. Fluids **6**, L042001 (2021).

[22] T. Mai, C. Mai, A. Raby, and D. M. Greaves, Aeration effects on water-structure impacts: Part 1. drop plate impacts, Ocean Eng. **193**, 106600 (2019).

[23] T. Mai, C. Mai, A. Raby, and D. M. Greaves, Hydroelasticity effects on water-structure impacts, Exp. Fluids **61**, 191 (2020).

[24] B. C. Abrahamsen, H. S. Alsos, V. Aune, E. Fagerholt, O. M. Faltinsen, and Φ. Hellan, Hydroplastic response of a square plate due to impact on calm water, Phys. Fluids **32**, 082103 (2020).

[25] S. H. Oh, S. H. Kwon, and J. Y. Chung, A close look at air pocket evolution in flat impact, in *Proceedings of the 24th International Workshop on Water Waves and Floating Bodies* (Zelenogorsk, Russia 2009), pp. 19–22.

[26] E. V. Ermanyuk and N. V. Gavrilov, Experimental study of disk impact onto shallow water, J. Appl. Mech. Tech. Phys. **52**, 889 (2011).

[27] S. Tödter, O. el Moctar, J. Neugebauer, and T. E. Schellin, Experimentally measured hydroelastic effects on impact-induced loads during flat water entry and related uncertainties, J. Offshore Mech. Arct. Eng. **142**, 011604 (2020).

[28] H. Xie, H. L. Ren, S. Qu, and H. Y. Tang, Numerical and experimental study on hydroelasticity in water-entry problem of a composite ship-hull structure, Compos. Struct. **201**, 942 (2018).

[29] C. W. Hirt and B. D. Nichols, Volume of fluid (VOF) method for the dynamics of free boundaries, J. Comput. Phys. **39**, 201 (1981).

[30] Q. L. Qu, M. X. Hu, H. Guo, P. Q. Liu, and R. K. Agarwal, Study of ditching characteristics of transport aircraft by global moving mesh method, J. Aircr. **52**, 1550 (2015).

[31] T. Miyamoto and K. Tanizawa, A study of the impact load on ship bow, J. Soc. Nav. Archit. Jpn. **1984**, 297 (1984).

[32] S. Tavakoli, T. Mikkola, and S. Hirdaris, A fluid–solid momentum exchange method for the prediction of hydroelastic responses of flexible water entry problems, J. Fluid Mech. **965**, A19 (2023).

[33] A. Aghaei, S. Schimmels, T. Schlurmann, and A. Hildebrandt, Numerical investigation of the effect of aeration and hydroelasticity on impact loading and structural response for elastic plates during water entry, Ocean Eng. **201**, 107098 (2020).